



Publication Year	2019
Acceptance in OA @INAF	2020-12-30T11:13:44Z
Title	Using Independent Component Analysis to Detect Exoplanet Reflection Spectrum from Composite Spectra of Exoplanetary Binary Systems
Authors	DI MARCANTONIO, Paolo; MOROSI, Carlo; FRANCHINI, Mariagrazia; Lehmann, Holger
DOI	10.3847/1538-3881/ab3e71
Handle	http://hdl.handle.net/20.500.12386/29354
Journal	THE ASTRONOMICAL JOURNAL
Number	158



Using Independent Component Analysis to Detect Exoplanet Reflection Spectrum from Composite Spectra of Exoplanetary Binary Systems

Paolo Di Marcantonio¹ , Carlo Morossi¹ , Mariagrazia Franchini¹ , and Holger Lehmann² 

¹INAF—Osservatorio Astronomico di Trieste, Via G. B. Tiepolo 11, Trieste, I-34143, Italy; paolo.dimarcantonio@inaf.it

²Thüringer Landessternwarte Tautenburg, Sternwarte 5, D-07778 Tautenburg, Germany

Received 2019 June 12; revised 2019 August 23; accepted 2019 August 25; published 2019 September 27

Abstract

The analysis of the wavelength-dependent albedo of exoplanets represents a direct way to provide insight into their atmospheric composition and to constrain theoretical planetary atmosphere modeling. Wavelength-dependent albedo can be inferred from the exoplanet’s reflected light of the host star, but this is not a trivial task. In fact, the planetary signal may be several orders of magnitude lower (10^{-4} or below) than the flux of the host star, thus making its extraction very challenging. Successful detection of the planetary signature of 51 Peg b has been recently obtained by using cross-correlation function or autocorrelation function techniques. In this paper we present an alternative method based on the use of Independent Component Analysis (ICA). In comparison to the above-mentioned techniques, the main advantages of ICA are that the extraction is “blind” i.e., it does not require any a priori knowledge of the underlying signals, and that our method allows us not only to detect the planet signal but also to estimate its wavelength dependence. To show and quantify the effectiveness of our method we successfully applied it to both simulated data and real data of an eclipsing binary star system. Eventually, when applied to real 51 Peg + 51 Peg b data, our method extracts the signal of 51 Peg but we could not soundly detect the reflected spectrum of 51 Peg b mainly due to the insufficient signal-to-noise ratio of the input composite spectra. Nevertheless, our results show that with “ad hoc” scheduled observations an ICA approach will be, in perspective, a very valid tool for studying exoplanetary atmospheres.

Unified Astronomy Thesaurus concepts: [Astronomical methods \(1043\)](#); [Exoplanet detection methods \(489\)](#); [Radial velocity \(1332\)](#); [Exoplanet atmospheres \(487\)](#); [Binary stars \(154\)](#); [Astronomical techniques \(1684\)](#)

1. Introduction

Observations of spectra of stars with exoplanets are a fundamental tool to determine not only the basic orbital parameters of surrounding planets but also to get hints on their atmosphere (if any). In fact, spectroscopic observations contain the variations of Doppler shifts of spectral lines of both components, i.e., star and planet(s), caused by changes of their radial velocities during their orbital motion (for discussion about radial velocity see Lindegren & Dravins 2003). Furthermore, the radius and the mass of exoplanets can be derived by combining the light-curve signal of exoplanetary transits with radial velocities using Kepler laws.

To derive information on exoplanet albedo and spectrum, we need to distinguish, in the observed (composite) spectra, the spectral features belonging to individual system components, i.e., to decompose the observed superposition of their lights. Since information on the individual spectra of the observed system is entangled in the composite spectra, the procedure of decomposing them is often referred to as disentangling. Disentangling can be performed by comparing spectra taken at different known radial velocities of the star and of the exoplanet or at phases with different known light ratios (e.g., during transit and/or eclipse). These approaches are also at the basis of the studies of binaries (see for example the discussion by Hadrava 2016, and references therein).

In the case of an exoplanet, the reflected spectral signal from its atmosphere, which should mimic the stellar signal, enables us to gather the planetary albedo and thus information on its atmospheric composition. In fact, the planetary reflectivity depends on wavelength because of scattering and absorption processes that suffer the incoming radiation in its atmosphere

and/or surface. The subject of modeling and understanding the planetary atmospheric structure from the reflected and emitted spectra is very complex, and there are many different approaches (see an overview of the problem in Marley & Robinson 2015 and a more detailed review in Marley et al. 2013). Moreover, the determination of the planetary albedo is not a simple task from the observational point of view because of the extremely low flux ratio between the reflected light from the planet and the stellar one. As examples of the several efforts to derive exoplanetary albedos we recall Charbonneau et al. (1999), Collier Cameron et al. (1999), and Rodler et al. (2010). In most of the cases the authors were able to establish only upper limits for the reflected signals. Recently a significant improvement has been obtained by means of new *ad hoc* techniques. Martins et al. (2013) proposed a technique that makes use of the Cross Correlation Function (CCF) of high resolution spectra to amplify the planetary signal above stellar noise and detected the reflected signal of 51 Peg b. Moreover, Martins et al. (2018) showed, by using simulated data, that the CCF method can successfully recover the geometric albedo of exoplanets over a wavelength range. Borra & Deschatelets (2018) suggested the use of autocorrelation function (ACF) as a valid alternative to CCF, in particular because it does not require a weighted binary mask. Both techniques search for secondary maxima in the CCF or ACF of the composite spectra due to the presence of a Doppler shifted reflected light signal.

In this paper we propose an alternative technique to both CCF and ACF that uses the Independent Component Analysis (ICA; Hyvärinen et al. 2001) as an effective way to disentangle the exoplanetary signal from instrument and stellar components. ICA is a method for extracting hidden components from multivariate statistical data that are both statistical independent

and non-Gaussian (see Section 2.3). The use of ICA in this paper is based on the assumption that the individual spectra forming the composite spectrum of the stellar-planet system can be considered as two independent components (see Section 3 for discussion). Since ICA was initially proposed to solve the blind source separation (BSS) problem, one of the main characteristics of our method, hereafter Exoplanet Reflected Light via Independent Component Analysis (ERLICA), lies in the fact that it does not require any *a priori* auxiliary information but only the observed data themselves. Furthermore, our method not only enables us to detect a planetary signal but is also able to provide, if the signal-to-noise ratio (S/N) of the input spectra is enough, the variation of the planet albedo with wavelength.

The goal of this work is to assess and analyze the efficiency of our method in detecting a planetary signal and in estimating its wavelength dependency by means of reflected starlight. To do so, we apply ERLICA to both artificial (simulated) and real (observed) spectra in the same optical region studied by Martins et al. (2015) and by Borra & Deschatelets (2018) in order to be able to compare our and their results. Obviously, the same kind of analysis could have been applied to other wavelength regions, e.g., to IR or UV data.

In Section 2 we summarize the theoretical framework of an exoplanetary system and give a short description of the ICA packages (FastICA³ and ICASSO⁴) we use. Section 3 describes the adopted method and its validation by using simulated data for the 51 Peg + 51 Peg b system. Section 4 shows and discuss the results of our methodology applied to the real (observed) case of the binary eclipsing star R CMa (an Algol system) and of 51 Peg + 51 Peg b system. Conclusions are given in Section 5.

2. Theoretical Framework

2.1. Exoplanet's Reflected Light

The model adopted in this paper to simulate the photometric variations of the stellar light reflected from a planet orbiting its host star is based on the discussion presented in Charbonneau et al. (1999) and reused by Martins et al. (2013). The phase-dependent flux ratio of the planet flux F_{planet} relatively to the star flux F_{star} is given by

$$\frac{F_{\text{planet}}(\alpha)}{F_{\text{star}}} = pg(\alpha) \left(\frac{R_p}{a} \right)^2 \quad (1)$$

where p is the geometric albedo of the planet, R_p is the planet radius, a is the planet orbital distance and $g(\alpha)$ is the phase function. It holds for the case $R_p \ll R_{\text{star}} \ll a$. As described in Borra & Deschatelets (2018), the phase angle, α , is the angle between the star and the Earth when seen from the planet. It depends on the position of the planet in its orbit and takes a value in the range $0 \leq \alpha \leq 180^\circ$. For an orbital inclination i and orbital phase ϕ , assuming a circular orbit, α can be derived from

$$\cos(\alpha) = -\sin(i)\cos(2\pi\phi). \quad (2)$$

The orbital phase ϕ in Equation (2) traces the position of the planet on its orbit around the star. ϕ takes values between 0 and 1. In Charbonneau et al. (1999) it is assumed 0 at the time of

maximum radial velocity, in other works (e.g., Borra & Deschatelets 2018), phase 0 corresponds to the time of the mid-point of the transit. In this paper we will use the latter definition, i.e., for us $\phi = 0$ at the mid-point of the transit or of the inferior conjunction. For this particular choice, at a given time t , ϕ value can be calculated knowing the planet time of transit t_0 and its orbital period P_{orb} by

$$\phi = \frac{t - t_0}{P_{\text{orb}}}. \quad (3)$$

The phase function $g(\alpha)$ in Equation (1) models the fraction of the maximum planet's reflected flux at full phase. It varies, depending on the planet position on its orbit, since we see a different portion of the planet illuminated hemisphere. As described in Langford et al. (2011), in the simplest case, we can assume an isotropic scattering over 2π sr (Lambert-law sphere) in which case $g(\alpha)$ has typically the form

$$g(\alpha) = \frac{[\sin(\alpha) + (\pi - \alpha)\cos(\alpha)]}{\pi} \quad (4)$$

and α is related to orbital phase ϕ as described by Equation (2).

The geometric albedo p , which appears in Equation (1), is the reflectivity of a planet measured at superior conjunction. It is a wavelength-dependent, dimensionless number, with values between 0 and 1 obtained as a ratio between the reflected and incident flux.

2.2. Exoplanet's Radial Velocity

The radial velocity equations describing the system are

$$RV_{\text{star}} = \gamma + K_{\text{star}}[\cos(\omega + f) + e \cos(\omega)] \quad (5)$$

and

$$RV_{\text{planet}} = \gamma - K_{\text{planet}}[\cos(\omega + f) + e \cos(\omega)] \quad (6)$$

for the star and the planet respectively. γ corresponds to the system's barycenter radial velocity relatively to the Sun, ω is the argument of periastron, e is the eccentricity, and f is the true anomaly; K_{star} and K_{planet} are the radial velocity semi-amplitude of, respectively, the stellar and planetary orbits and can be computed from the orbital parameters as

$$K_{\text{star}} = \frac{2\pi a}{P_{\text{orb}}} \frac{m_{\text{planet}}}{m_{\text{star}} + m_{\text{planet}}} \frac{\sin i}{\sqrt{1 - e^2}} \quad (7)$$

$$K_{\text{planet}} = \frac{2\pi a}{P_{\text{orb}}} \frac{m_{\text{star}}}{m_{\text{star}} + m_{\text{planet}}} \frac{\sin i}{\sqrt{1 - e^2}} \quad (8)$$

where m_{star} and m_{planet} are the two masses of the star and planet, respectively. The true anomaly f , as a function of time t can be computed (see for example Mortier et al. 2016) from

$$\tan \frac{f}{2} = \sqrt{\frac{1 + e}{1 - e}} \tan \frac{E}{2} \quad (9)$$

where E , the eccentric anomaly, can be found solving the Kepler equation

$$E - e \sin E = 2\pi \frac{t - t_0}{P_{\text{orb}}}. \quad (10)$$

Knowing ϕ , the planet radial velocity relative to the star can be obtained as the difference between RV_{planet} and RV_{star} which

³ <https://research.ics.aalto.fi/ica/fastica/>

⁴ <https://research.ics.aalto.fi/ica/icasso/>

could be also written as (see Charbonneau et al. 1999)

$$RV_{\text{planet,star}} = -K_{\text{star}} \frac{m_{\text{star}} + m_{\text{planet}}}{m_{\text{planet}}} \sin(2\pi\phi). \quad (11)$$

This velocity can be used to compute the Doppler wavelength shift between the stellar and planet spectra at each ϕ in Equation (15).

2.3. ICA Technique

The ICA technique was initially proposed to solve the BSS problem. In the BSS problem the task is to separate unknown individual signals (sources or also components) from mixtures of signals without a priori knowledge of the mixing process. In ICA, as the name implies, the basic goal is to find a linear transformation in which the underlying components are statistically as independent from each other as possible. ICA differs from the more common approach to component separation provided by Principal Component Analysis (PCA) which performs a linear transformation of the data to obtain mutually uncorrelated, orthogonal directions, called indeed principal components. If the hidden signals under investigation follow Gaussian distributions, uncorrelatedness is equivalent to mutual independence and algorithms such as PCA are able to separate them. However if the signals follow a non-Gaussian distribution (and most astronomically observed signals are predominantly non-Gaussian), it can be shown that uncorrelated signals are not necessarily mutually independent and hence methods like PCA fail to optimally separate individual components (Waldmann 2012). It is actually here where ICA-based separation methods could be of interest.

A comprehensive description of the ICA technique can be found in Hyvärinen et al. (2001). Hereafter we just recall that in ICA the model for the data can be expressed as

$$\mathbf{X} = \mathbf{A}\mathbf{S}, \quad (12)$$

where $\mathbf{X} = (x_1, x_2, \dots, x_m)^T$ are the observed m mixtures, $\mathbf{S} = (s_1, s_2, \dots, s_n)^T$ are the latent variables (i.e., components) that cannot be observed and \mathbf{A} is an unknown constant $m \times n$ matrix, called the mixing matrix. We use bold upper-case letters to denote matrices and lower-case letters (for example x_1) to denote, instead, vectors.

The challenge is to estimate the mixing matrix and its (pseudo) inverse de-mixing matrix, $\mathbf{W} = \mathbf{A}^{-1}$, without any additional prior knowledge of either \mathbf{A} and \mathbf{S} . The estimation of the matrix \mathbf{S} with the knowledge of \mathbf{X} is the linear source separation problem and can be achieved by maximizing some measure of independence. Several of such measures are used, like kurtosis, negentropy, or mutual information (Hyvärinen et al. 2001) and a large variety of algorithms implementing the above mentioned independence measures (e.g., Second Order Blind Identification, SOBI, Belouchrani et al. 1997; Joint Approximation Diagonalization of Eigenmatrices, JADE, Cardoso & Souloumiac 1993; fixed-point algorithm, FastICA, Hyvärinen 1999 and many others see Waldmann 2012) exists.

2.3.1. FastICA

In the present work we decided to use the FastICA algorithm since it is one of the fastest, most commonly used and it is well documented. It is also available in many programming languages and, in particular, we use the FastICA package for

MatlabTM. A detailed description of the algorithm can be found in Hyvärinen (1999). Here we just recall its main steps:

1. data are centered (set them at mean zero);
2. data are whitened (i.e., \mathbf{X} data are transformed so that the components of the new vector $\tilde{\mathbf{X}}$ are uncorrelated and their variances equal to unity);
3. the inverse de-mixing matrix \mathbf{W} is estimated;
4. the mixing matrix \mathbf{A} and the component matrix \mathbf{S} are computed.

The matrix \mathbf{W} is estimated row by row with the following iterations scheme:

- (a) choose initial (random) weight vector w_i
- (b) let $w_i^+ = E[\mathbf{X}g(w_i^T \mathbf{X})] - E[g'(w_i^T \mathbf{X})]w_i$, where g and g' are the derivatives of the chosen contrast function (see Equation (13))
- (c) normalize w_i^+
- (d) repeat step (b) and (c) until convergence is achieved

where convergence means that the old and new values of w_i point in the same direction, i.e., their dot-product is (almost) equal to 1.

A contrast function G and its first and second derivatives, g and g' , are generally used to approximate the negentropy of the system. In our FastICA package, the choice is restricted to the following functions:

$$\begin{aligned} G_1(u) &= \frac{1}{a_1} \log \cosh(a_1 u) \\ G_2(u) &= -\exp(-u^2/2) \\ G_3(u) &= \frac{1}{4} u^4. \end{aligned} \quad (13)$$

The problem of most ICA algorithms is that they are based on methods related to gradient descent where the basic principle is to start in some initial point, and then make steps in a certain direction until a convergence criterion is met. In the case of the FastICA sequence the w_i initial vector of weights is generated at random and the algorithm stability is therefore not always deterministic. Moreover, it is known that Equation (12) led to two ambiguities:

1. sign and variances of the independent components could not be determined;
2. order of independent components could also not be determined.

Both ambiguities are directly related to the fact that both \mathbf{A} and \mathbf{S} are unknown. Any scalar multiplier in one of the components s_i could always be canceled by dividing the corresponding column a_i of \mathbf{A} by the same scalar. FastICA assumes that each component has unit variance and correspondingly the matrix \mathbf{A} is adapted to take into account this restriction; this solves point 1 apart for a sign ambiguity. Concerning the order, positions of independent components can be freely changed without affecting the Equation (12). To show this, it is enough to reshuffle Equation (12) by multiplying it with a permutation matrix \mathbf{P} and its inverse as $\mathbf{X} = \mathbf{A}\mathbf{P}^{-1}\mathbf{P}\mathbf{S}$. The matrix $\mathbf{A}\mathbf{P}^{-1}$ is the new unknown mixing matrix with order of column position changed. A way to mitigate the FastICA instability and ambiguities is to run ICA algorithms many times and measure “somehow” the stability of the obtained components. This is the purpose of ICASSO, a software package aiming at investigating the relations among estimates from FastICA both programmatically as well as visually.

2.3.2. ICASSO

The ICASSO method is described in Himberg et al. (2004) and is based on estimating a large number of candidate independent components by running the FastICA algorithm many times, and visualizing their clustering in the signal space. If an independent component is reliable (almost) every run of the algorithm should produce one point in the signal space that is very close to the “real” component. Thus, reliable independent components correspond to clusters that are small and well separated from the rest of the estimates. In contrast, unreliable components correspond to points which do not belong to any cluster.

In ICASSO, independent component estimates can be computed either by randomizing initial condition or by bootstrapping. In the first case, FastICA is run M times (M , user definable number of iterations) on the same data X , but starting each time with a new random initial condition; in the second case, the M runs are performed keeping the same initial condition, but the data are re-sampled by bootstrapping them every time. Obtained estimates at each run are afterwards clustered according to their mutual similarities (agglomerative clustering with average-linkage criterion is actually used), visualized in a 2D plot and made available through a dedicated application programming interface for successive analysis.

In ICASSO the clustering performed by the software package is already capable of grouping similar components obtained over the many, user-defined, runs, based on the absolute value of their mutual correlation coefficients (for details see Himberg et al. 2004). Despite the ambiguities described in 2.3.1, the similarity criterion allows us to integrate estimates of all the runs in a new single estimate, called in ICASSO, “centrotype”. Basically it is the point in the cluster that has the maximum sum of similarities (as measured by correlation coefficients) with respect to the other points in the cluster. The obtained estimates therefore not only can be considered “reliable”, but also “improved”, if compared with a single FastICA run.

The coupling of the ICASSO package with the FastICA one in the MatlabTM environment was also one of the drivers to select specifically the FastICA algorithm among the various ICA algorithms described in the literature.

3. Method Description and Validation

In the present work we want to apply ERLICA to decompose an observed spectrum produced by an exoplanetary system (star plus one planet) in individual components. The observed mixture X matrix is, in this case, composed by the x_j (observed) spectra, where $x_j = x_j(\lambda_0, \dots, \lambda_l)$ represents one realization out of m (observed) spectra, whereas the 2 individual components that we want to extract, s_1 and s_2 , are the stellar and exoplanet spectra. Note that for non-overcomplete sets the number of (observed) spectra should be equal to the individual source signals (i.e., $m = 2$ for our specific case). For overcomplete sets (i.e., more data than source signals) dimensionality can be reduced given some selection criteria (e.g., S/N, in the case of stellar spectra, or others) thus reducing the set to the non-overcomplete case.

Before applying our ERLICA method to real observations we decided to test it on artificial (simulated) data in order to be able to assess its effectiveness and validity. Following the notation of Equation (1) we will identify hereafter s_1 as F_{star} , s_2 as F_{planet} and individual (observed) spectra as $F_j(\lambda)$. The

Table 1
Nominal Orbital Parameters for 51 Peg + 51 Peg b System

Orbital parameter	Value	Reference
t_0	2456021.256 JD	Martins et al. (2015)
P_{orb}	4.231 day	Martins et al. (2015)
m_{star}	1.12 M_{Sun}	Fuhrmann et al. (1997)
m_{planet}	0.46 M_J	Martins et al. (2015)
a	0.052 au	Martins et al. (2015)
i	80 deg	Martins et al. (2015)
ω	0	Martins et al. (2015)
γ	-33.152	Martins et al. (2015)
R_{star}	1.20 R_{Sun}	Fuhrmann et al. (1997)
R_p	1.9 R_J	Martins et al. (2015)

validity of using ICA relies on the assumption that F_{star} and F_{planet} are independent while its effectiveness should be related to the S/N of the input data. Statistical independence of F_{star} and F_{planet} means that, at each wavelength, $F_{\text{planet}}(\lambda_i)$ does not depend on $F_{\text{star}}(\lambda_i)$. In our case, this can be expected due to the relative Doppler shift of the two spectra and to the modulation introduced by the albedo. A qualitative indication of independence can be inferred by looking at the soundness of the results of applying ERLICA to simulated data. In fact, only if the independence assumption is valid, would ERLICA be able to provide reliable results.

Since, in the case of real statistical independence, the joint pdf (probability density function) is factorizable into the product of the single marginal pdfs, a further quantitative indication can be assessed by checking the similarity between the frequency distributions $f(F_{\text{star}}|F_{\text{planet}})$ and $f(F_{\text{star}}) \times f(F_{\text{planet}})$. Actually, we found that their average difference, $\langle f(F_{\text{star}}|F_{\text{planet}}) - f(F_{\text{star}} \times f(F_{\text{planet}})) \rangle$, is equal to zero within 2σ (see results in Section 3.1), thus confirming the “practical” independence of F_{star} and F_{planet} .

It is important to note that in general the observed signal is a sum of the two astrophysical signals and of various, even complex, sources of noise and it is characterized by its S/N. To take into account in our simulation the S/N role, we mimic, without losing in generality, only the case of pure Gaussian noise ignoring systematics introduced by several causes like instrumental signature, stellar activity, telluric fluctuations etc. (see discussion in Waldmann et al. 2013). In fact at the level of simulation, adding additional non-Gaussian systematic components will not add new information to the problem of component separations since, due to its nature, ICA will be able to disentangle them anyway. On the contrary, adding specific systematics will require us to tie simulations to a specific instrument (which we would like to avoid to stay general) and force us to use a more complex observed matrix (with as many rows as the component we would like to search for).

3.1. Simulation of an Exoplanetary System: The Case of 51 Peg b

To represent a possible real case, we decided to simulate the 51 Peg + 51 Peg b planetary system. Indeed, this is also one of the first systems where reflected signal from an exoplanet has been detected at a significance of $3\sigma_{\text{noise}}$ (Martins et al. 2015). To properly characterize the system we use the parameters summarized in Table 1.

The model of the composite spectrum at different orbital phases is obtained, similarly as it was done in Borra &

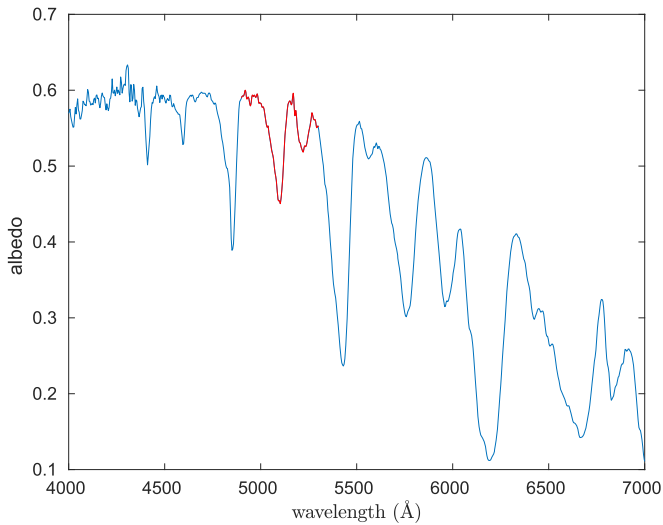


Figure 1. Full-disk albedo of Neptune as obtained by Karkoschka (1998); red portion of the albedo highlights the wavelength range used in the paper.

Deschatelets (2018), by adding to a stellar spectrum the same spectrum Doppler shifted and modulated by:

1. a phase-dependent function
2. the predicted geometric flux ratio of the planet relative to the star
3. a reflecting albedo

as described in Sections 2.1 and 2.2.

In order to simulate the composite spectrum, we used as $F_{\text{star}}(\lambda)$ the synthetic spectrum of 51 Peg computed by means of SPECTRUM v.276e (Gray & Corbally 1994) starting from an ATLAS12 atmosphere model (Kurucz 2005) at $T_{\text{eff}} = 5787$ K, $\log g = 4.45$ dex, metallicity 0.15 dex and microturbulence 0.85 km s^{-1} (data taken from Valenti & Fischer 2005). The synthetic spectrum was broadened to take into account the rotational velocity of 2.6 km s^{-1} , macroturbulence velocity of 3.95 km s^{-1} and degraded at the resolution of ESO HARPS spectrograph ($R \approx 115,000$). The same synthetic spectrum, but Doppler shifted, was used to compute the $F_{\text{planet}}(\lambda)$. The planetary albedo $p(\lambda)$ was assumed to be equal to the Neptune one given by Karkoschka (1998) and it is shown in Figure 1. More recent measurements by Madden & Kaltenecker (2018) are also available in the literature, but we decided to use the ones by Karkoschka (1998) due to their more extended wavelength coverage toward the blue. We decided to use the Neptune albedo because in the wavelength range of our simulation it shows prominent features with variations of the order of $\pm 30\%$. The goodness of our method in extracting planet features can be in this way better assessed. Actually at the level of simulation what is important is to show the ability to recover the planet signal given in input; in principle, without any loss in generality, we could even not use any real, observed albedo, but simply adopt for $p(\lambda)$ a monotonic function.

In our simulation the spectra are limited to the $4900\text{--}5300 \text{ \AA}$ wavelength range and have a fixed step of 0.005 \AA . The wavelength range has been chosen in a spectral region where there is a possibility of achieving good S/N in the case of real ground-base observations avoiding regions of telluric contamination and the presence of strong lines (e.g., hydrogen ones), yet keeping the computational time reasonable.

To create the synthetic observed mixture X (composed by different $F_j(\lambda)$), to be analyzed subsequently by ICA, one should note that it is not possible to use $F_j(\lambda)$ for all different ϕ simultaneously. In fact, the contribution of the $F_{\text{planet}}(\lambda, \phi)$ in each $F_j(\lambda)$, at different phase angles, would be seen by ICA as a different independent component (due to the different radial velocity shift). This will lead to an attempt to disentangle an observed mixture X composed, say, by $mF_j(\lambda)$ in $n = m + 1$ components i.e., $m F_{\text{planet}}(\lambda, \phi)$ and one F_{star} , which has of course, no solution. We actually need to inject in ICA an observed mixture such that the dimensionality is correctly preserved. For our specific exoplanetary case this can be achieved, in the most simple case, by using a pair of spectra $F_j(\lambda)$ where in one of them the exoplanet reflected spectrum is not present. The observed mixture X assumes in this case the form:

$$X = \begin{pmatrix} F_1(\lambda) \\ F_2(\lambda) \end{pmatrix} \quad (14)$$

where:

$$\begin{aligned} F_1(\lambda) &= F_{\text{star}}(\lambda) \\ F_2(\lambda, \phi) &= F_{\text{star}}(\lambda) + F_{\text{planet}}(\lambda, \phi) \\ &= F_{\text{star}}(\lambda) + p(\lambda) \left[\frac{R_{\text{planet}}}{a} \right]^2 g(\alpha) F_{\text{star}} \\ &\quad \times \left(\lambda \left[1 + \frac{RV_{\text{planet,star}}}{c} \right] \right). \end{aligned} \quad (15)$$

In Equation (15), $\phi \in [0, 1]$ is the usual orbital phase (see Equation (3)) and $RV_{\text{planet,star}}$ is the radial velocity of the planet relative to that of the star (as derived in Equation (11)). $F_1(\lambda)$ thus effectively represents a spectrum obtained at the planet occultation ($\phi = 0.5$) if it is an eclipsing system, or at the inferior conjunction ($\phi = 0.0$) if not, i.e., when no starlight is reflected by the planet toward the observer. $F_2(\lambda)$, instead, contains also the contribution reflected by the planet at the corresponding phase ϕ . As discussed in Section 3 to check the independence of F_{star} and F_{planet} we computed $f(F_{\text{star}}|F_{\text{planet}})$ and $f(F_{\text{star}}) \times f(F_{\text{planet}})$ and we found an average difference, $\langle f(F_{\text{star}}|F_{\text{planet}}) - f(F_{\text{star}}) \times f(F_{\text{planet}}) \rangle$, equal to $2.7 \times 10^{-6} \pm 2.1 \times 10^{-6}$. Such a low difference suggests that the two spectra are independent and thus we can be confident that ERLICA will be able to extract the two searched components, i.e., the stellar spectrum and the reflected light from the exoplanet properly modulated by the introduced albedo.

In order to simulate a realistic case, as discussed in Section 3, we added to both spectra realizations, by using MatlabTM function *normrnd*, a Gaussian noise with mean zero and standard deviation $F(\lambda)/S/N$ (where S/N is a parameter to specify the S/N of the $mF_j(\lambda)$ spectra in the wavelength range of interest). Expressing the noise via S/N is convenient and allows us to estimate the validity of the obtained results as a function of varying S/N.

3.1.1. Extraction of ICA Components

In order to assess the behavior of ICA in disentangling the system individual components we started by applying ERLICA, i.e., FastICA+ICASSO, on the composite spectra obtained when 51 Peg and 51 Peg b are at the two phases presented in Figure 2. These configurations represent somehow the two competing “extreme” cases: the case of maximum available flux signal and still different planet and stellar radial

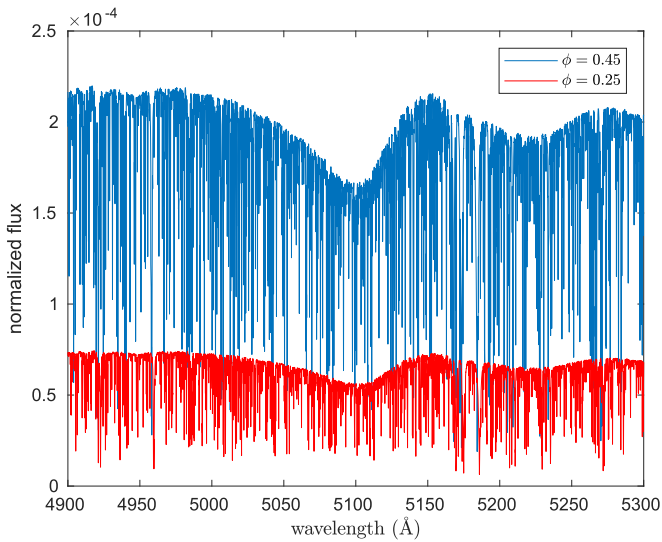


Figure 2. Simulated reflected spectrum of 51 Peg b at two different orbital phases ϕ : $\phi = 0.45$ (blue line) corresponding to the case of maximum reflection (planetary disk almost fully illuminated) and at $\phi = 0.25$ (red line) corresponding to the case of maximum separation in radial velocity.

velocities versus the maximum shift in radial velocity but a lower phase dependent flux ratio. The blue spectrum in the figure corresponds to the case of the exoplanet disk almost fully illuminated, $\phi = 0.45$, but with a minimal separation in radial velocity ($RV_{\text{planet,star}} \approx 40.7 \text{ km s}^{-1}$). In this case, the phase dependent flux ratio (see Equation (1)) amounts to 2.9×10^{-4} . The red spectrum, on the contrary, represents the case of maximum shift in radial velocity ($\phi = 0.25$, $RV_{\text{planet,star}} \approx 131.7 \text{ km s}^{-1}$), but with a disk only partially illuminated leading to a phase dependent flux ratio of 9.7×10^{-5} .

As a starting point a $S/N = 50,000$ has been adopted to limit the influence of the noise and highlight the capabilities of the method.

In extracting the two independent components we have to face the two ambiguities described in Section 2.3. The first one, i.e., the sign of each component, can be solved taking into account that each $F_2(\lambda, \phi)$ must be the sum of two positive quantities. Therefore we determined the sign of each disentangled component by taking into account the sign of the corresponding element of the matrix \mathbf{A} .

The second ambiguity, i.e. the order of the components, was resolved by comparing each of them with one of the two input spectra (each of them being dominated by the stellar signal) via cross-correlation. The output component with the highest value of the cross correlation is then labeled as component 1 and identified as the ICA estimate of F_{star} .

Setting up the simulation is however not enough: we need a way to judge and assess, with the results in hand, the “goodness” of ICA in extracting the two signals. We decided, therefore, to search for a quantitative, mathematical, estimator. A first attempt led us to calculate simply the standard deviation of the differences between the extracted components and the input F_{star} and F_{planet} . However, this estimator cannot be used in the case of real observations, since there will be no “a priori known” F_{star} and F_{planet} signals to be compared with. Therefore, we decided to use an approach similar to the one shown in Borra & Deschatelets (2018), i.e., to use, as a more reliable and feasible estimate, the peak intensity of the ACF of each obtained component. In fact, the higher this peak is, the

higher the strength of the detected signal is as discussed in Section 4.3 of Borra & Deschatelets (2018) who adopted a similar approach to assess the detection of a planetary signal with their ACF method.

Therefore, we autocorrelate each of the two found components extracted by applying ERLICA on the composite spectra. The ACFs are computed, after resampling the components on a velocity scale, by relatively shifting them at steps, lag, using a constant velocity increment. The ACF profile is, by construction, always symmetrical and well centered at 0 position. Actually, correlating a signal by itself always produces a peak centered at 0 and equal to 1 after normalization. If there is a signal, i.e., a detection, it can be inferred from the ACF increase with respect to the one obtained if only noise is present at X values (shifts) equidistant and close to 0 both on the negative and positive sides. Therefore, to use the ACF as an estimator we removed the autocorrelation peak at 0, which is, for our purposes, not meaningful and substitute it with a value given by interpolation (usually with a Gaussian fitting) of the neighborhood values. The peak intensity of such a modified profile can be used as a robust estimator of the detection level when compared with the same quantity obtained in the case of an ACF computed when a detection is not possible. No-detection can be simulated by injecting in ERLICA two spectra $F_1(\lambda)$ and $F_2(\lambda)$ computed both at $\phi \simeq 0.0$ thus using $F_{\text{planet}} = 0$ in Equation (15). In the following, we use the ratio of the peak of the ACF of each i component over the no-detection ACF peak value to define the detection significance, D_i , and declare that there is a detection, if D_i is larger than 3.

In summary the main steps of the simulation are the following:

- (i) create $F_1(\lambda)$ and $F_2(\lambda)$ according to Equation (15) for a chosen ϕ value;
- (ii) add to $F_1(\lambda)$ and $F_2(\lambda)$ a Gaussian noise to mimic spectra with different S/N values;
- (iii) create the observed mixture X and apply ERLICA;
- (iv) fix signs and order of the extracted components;
- (v) compute ACF of each component after re-sampling at steps of constant velocities;
- (vi) compute detection significance D_1 and D_2 values.

3.1.2. Contrast Function Selection and S/N Effect

FastICA algorithm implementation allows the user to choose between three different contrast functions (see Equation (13)). The theoretical analysis that led to the adoption of the aforementioned contrasts function can be found in Hyvarinen (1999); here we want just to recall the main conclusions given there:

1. $G_1(u)$ is a good general-purpose contrast function;
2. $G_2(u)$ may be better when robustness is very important;
3. $G_3(u)$ is not recommended in the case of presence of outliers.

To chose the most appropriate contrast function for our scientific case we applied the ERLICA approach as described in Section 3.1 by using all the three contrast functions and varying S/N on the simulated 51 Peg + 51 Peg b planetary system with $\phi = 0.45$. S/N has been varied in the range [1000–50,000] to span a noise amplitude interval from ten times to one fifth of the planet flux. For each value of S/N we

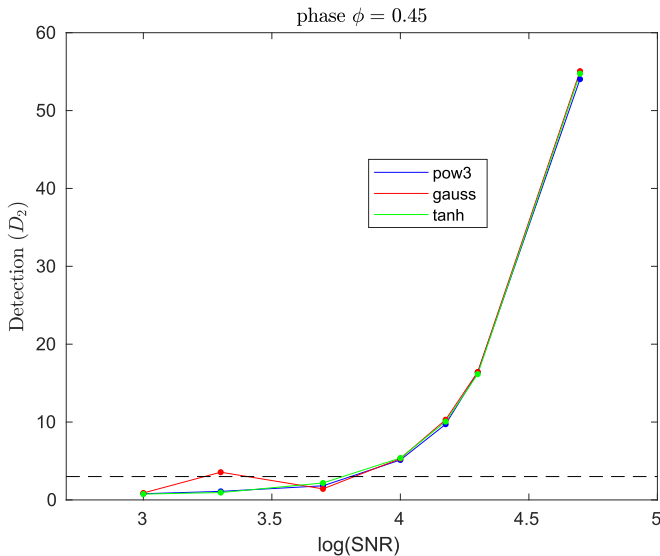


Figure 3. Trend of the detection significance for the second component as a function of the logarithm of S/N; different colors represent different adopted contrast functions while the dashed line corresponds to the detection threshold $D_2 = 3$ (see text).

computed the detection significance D_i of the disentangled components.

Figure 3 shows the results. Some points can be highlighted:

1. detection level increases with increasing S/N, as expected, independently of the adopted contrast function;
2. all the three contrast functions led to almost equivalent results, but for $S/N = 5000$. The $G_2(u)$ “gauss” contrast function shows a non-monotonic behavior for $S/N < 10,000$ which seems to indicate a greater sensitivity to the FastICA initial conditions;
3. in general a $S/N > 5000$ is required for a reliable detection ($D > 3$). This S/N limit corresponds to the case of a noise amplitude comparable to the planet signal one.

Taking into account the main conclusions in Hyvarinen (1999) and considering that $G_2(u)$ performs, sometimes, slightly better than the other contrast functions going toward low S/N we decided to use the $G_2(u)$ “gauss” contrast function in our ICA analysis. It is worthwhile noticing that, as shown in our simulations and highlighted in Hyvarinen (1999), this choice of the contrast function is not really critical in the sense that any of the contrast estimators in the FastICA framework works well for (practically) any distributions of the independent components (contrary to what happens in other ICA algorithms).

3.1.3. Simulation Results

First of all, we apply ERLICA at the case $\phi = 0$ where no detection of the second component is expected. The corresponding ACFs of the two component profiles are shown in Figure 4. In this case, ERLICA is clearly able to retrieve the first component, which has a well peaked ACF, whereas the ACF of the “second” one (actually ERLICA retrieves only noise) is flat and with a maximum value of about 0.01.

Then, we repeat the analysis for the case of maximum available reflected flux ($\phi = 0.45$) and for that of maximum shift in radial velocity ($\phi = 0.25$) between F_1 and F_2 . Figure 5

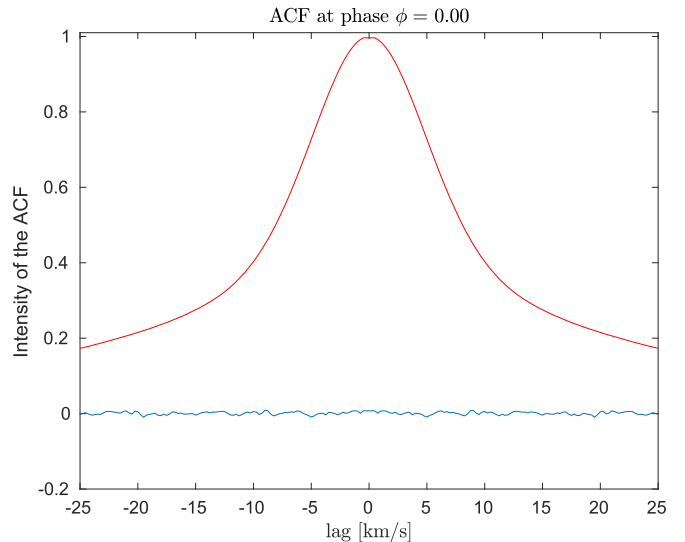


Figure 4. ACF profiles for the detected first component (red) and no-detected second one (blue), see text.

shows the first and second extracted components, and their ACFs, as obtained by our computation once FastICA is run with the Gaussian contrast function $G_2(u)$ (see Equation (13)), $S/N = 50,000$, and ICASSO with $M = 15$ iterations. In both cases, as can be seen already by a visual comparison, ICA is able to disentangle the two components (see (a), (c) and (b), (d) panels, respectively).

The comparison of the peaks of the ACF profiles, shown in panels (e) and (f), with the no-detection case shows that:

1. in the case of the maximum available flux both components are retrieved and reconstructed; peak of the ACF profiles for the first component is close to 1, thus the detection can be considered optimal ($D_1 \simeq 100$); the detection of the second component is lower ($D_2 \simeq 65$), but still the albedo trend is clearly noticeable in panel (c);
2. when the system is at $\phi = 0.25$ the retrieved second component is much more noisy (see panel (d)) and this is reflected by a decrease in the peak of the corresponding ACF profile. Nevertheless, also in this case the detection of the planet signal is achieved, $D_2 \simeq 20$.

Figure 6 shows results obtained by using a $S/N = 6500$ where the detection of the second component could still be considered achieved ($D_2 \simeq 3$). As shown in panel (c), the peak of the ACF profile for the second component (green curve) indeed still slightly exceeds our assumed limit of 3 for a reliable detection and confirms what was shown also in Figure 3. It is worth highlighting that, also in this case of much lower S/N, the first component (panel (a)) is still optimally retrieved ($D_1 \simeq 100$). On the other hand no conclusion can be inferred visually for the albedo wavelength dependency (see panel (b)) without applying some procedure of noise filtering.

In conclusion, our simulation results show that by using ERLICA we can effectively disentangle the individual components of a composite spectrum of an exoplanetary system like 51 Peg. For a composite spectrum with very high S/N (> 6500) we demonstrate that we can be able to detect the planet signal in a system with a flux ratio on the order of 10^{-4} . We also show that if the noise in the input spectra is of the order or smaller than the planet signal our method is also

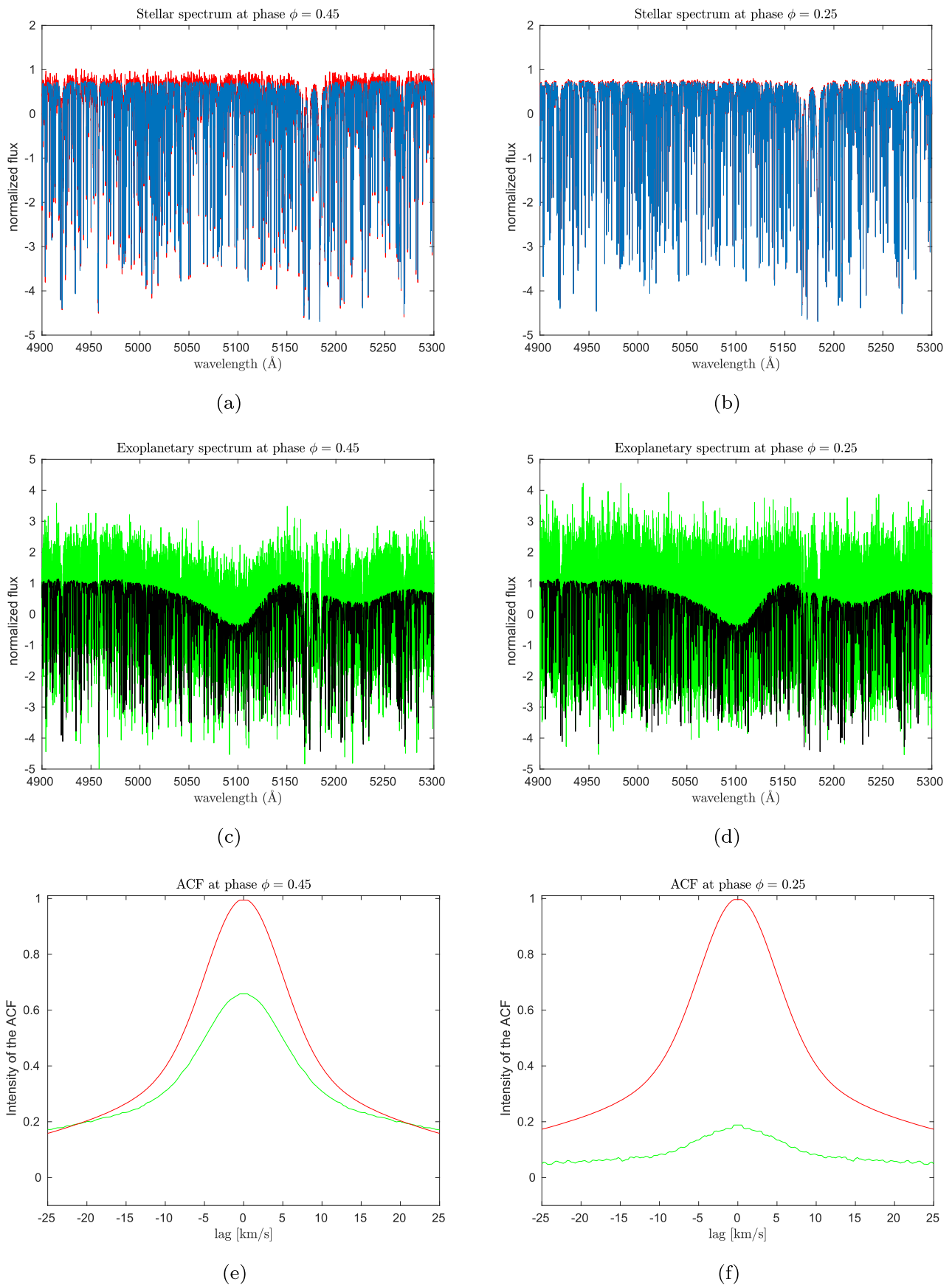


Figure 5. ICA results for $\phi = 0.45$ and $\phi = 0.25$, and $S/N = 50,000$. Panels (a) and (b): Detected first component (red) with superimposed the input star spectrum (blue); panels (c) and (d): Detected second component (green) with superimposed the input exoplanet reflection spectrum modulated by albedo (black); panels (e) and (f): ACF profiles of the first (red) and second (green) detected components.

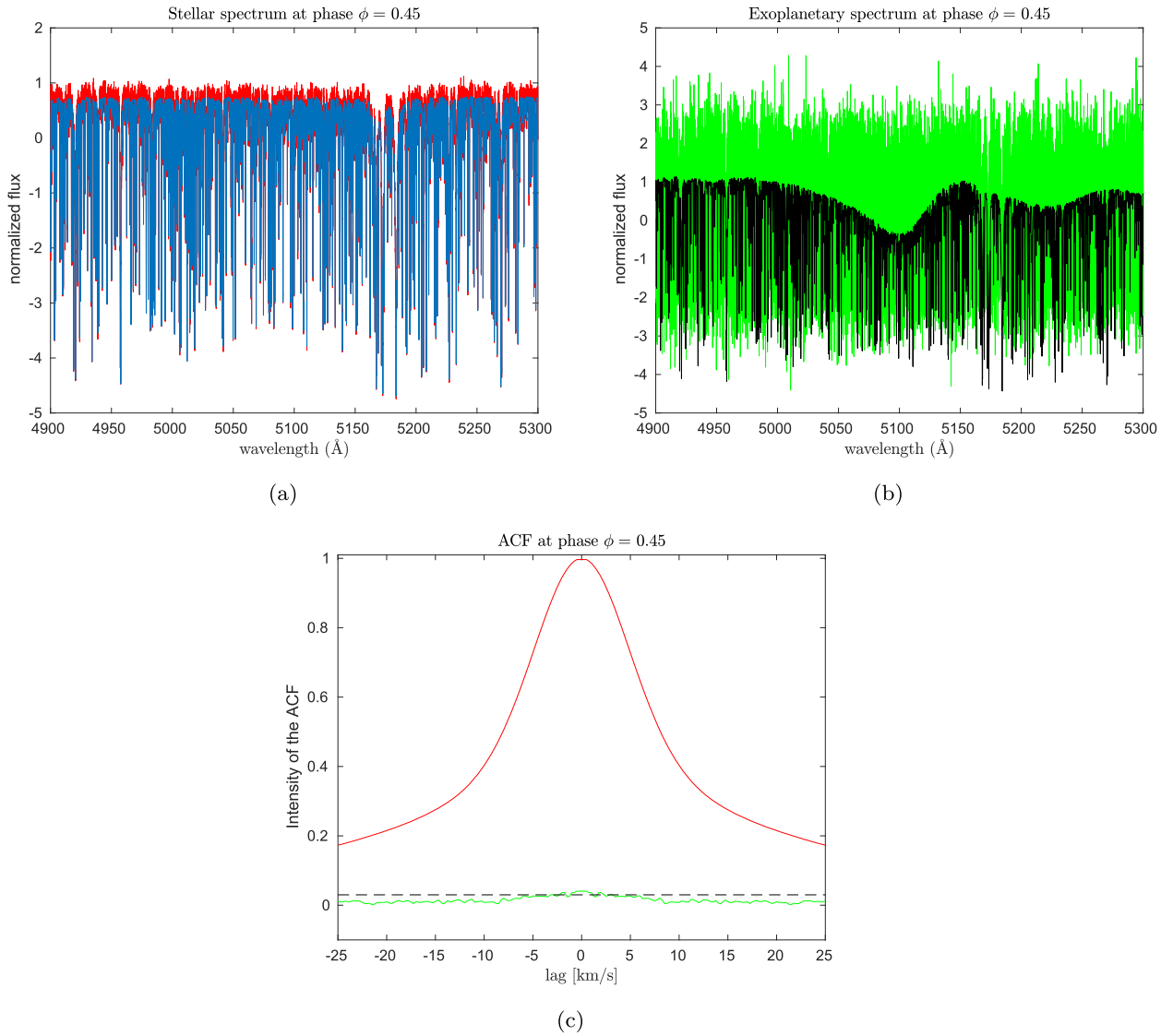


Figure 6. As Figure 5 for $\phi = 0.45$ and $S/N = 6500$. The dashed line corresponds to the detection threshold $D_2 = 3$.

capable of providing the planet reflected spectrum i.e., the albedo wavelength dependence without further processing. For lower S/N the estimate of the wavelength dependence of the planet reflected spectrum would require some extra processing to increase its S/N .

4. Results and Discussion

4.1. The Case of the Binary System RCMa

In order to test our method on real data we decided to look at the case of eclipsing binary stars which has the advantage of a higher flux ratio than in the case of an exoplanetary system. It should be noted indeed that for our approach the differences between an exoplanetary (binary) system and an eclipsing star (binary) system are really minor:

1. all the theoretical framework for radial velocity computation described in Section 2.2 applies, without losing in generality, to systems composed by two stars (basically, in the formulas it is enough to replace the subscript planet with star2);

2. all the photometric variations due to phase dependent reflected light (Section 2.1) are, on the contrary, not relevant and can be neglected but the two spectra $F_{\text{star1}}(\lambda)$ and $F_{\text{star2}}(\lambda)$ can still be considered as two independent components.

The observed mixture X in this case is composed by the following two signals:

$$\begin{aligned}
 F_1(\lambda) &= F_{\text{star1}}(\lambda) \\
 F_2(\lambda, \phi) &= F_{\text{star1}}(\lambda) + F_{\text{star2}}(\lambda, \phi) \\
 &= F_{\text{star1}}(\lambda) + F_{\text{star2}} \left(\lambda \left[1 + \frac{RV_{\text{star2}}(\phi) - RV_{\text{star1}}(\phi)}{c} \right] \right)
 \end{aligned}$$

where $F_1(\lambda)$ is the spectrum of the system in secondary eclipse, $0.45 < \phi < 0.55$ (i.e., a spectrum taken when the secondary star is hidden behind the primary), and $F_2(\lambda, \phi)$ is the combined spectrum of the primary and of the secondary obtained at $0.1 < |\phi| < 0.4$, thus avoiding the spectra taken during the primary eclipse where the problem of limb-darkening (see Winn 2010) and the Rossiter–McLaughlin (McLaughlin 1924; Rossiter 1924) effect modify the observed

Table 2
Stellar Parameters for R CMa System

Parameter	Value	Reference
$M_1 (M_\odot)$	1.67 ± 0.08	Budding & Butland (2011)
$M_2 (M_\odot)$	0.22 ± 0.07	Budding & Butland (2011)
q (mass ratio)	0.13 ± 0.05	Budding & Butland (2011)
$R_1 (R_\odot)$	1.78 ± 0.03	Budding & Butland (2011)
$R_2 (R_\odot)$	1.22 ± 0.07	Budding & Butland (2011)
T_{eff} (primary) (K)	7300	Budding & Butland (2011)
T_{eff} (secondary) (K)	4350	Budding & Butland (2011)
T_{eff} (primary) (K)	7033 ± 42	Lehmann et al. (2018)
T_{eff} (secondary) (K)	4350 ± 100	Lehmann et al. (2018)

$F_{\text{star}1}$. We recall that the $F_{\text{star}2}$ contribution to $F_2(\lambda, \phi)$ at each phase is Doppler shifted in wavelength because of the radial velocity of the secondary star with respect to the primary one. The required statistical independence of the two components hidden in the composite spectra is guaranteed because of the shift in radial velocity of the two stellar spectra and even reinforced by the fact that, in most astronomical cases, the two stars belong to different spectral classes and, therefore, have quite different spectra.

Out of the several eclipsing binary systems described in the literature we decided to study R CMa. The eclipsing binary star R CMa is a short-period Algol-type system showing an extraordinary small mass ratio between its components. R CMa was known for a long time as the system of lowest total mass and as the prototype of a small group of stars called the R CMa-type stars, introduced by Kopal (1956) and characterized by low mass ratio, overluminosity of the primary, and oversized secondary. Budding & Butland (2011) give a comprehensive overview of the history of the investigations of R CMa. They performed a combined photometric, astrometric, and spectroscopic analysis of the R CMa system and end up with the stellar parameters given in Table 2.

Lehmann et al. (2018) used time series of high-resolution spectra and analyzed the decomposed spectra of the components together with the radial velocities obtained from decomposed, least-squares deconvolved mean line profiles (LSD profiles, see Donati et al. 1997). Their results confirm the values given by Budding & Butland (2011) for the masses and radii, and also for the T_{eff} of the secondary component, whereas the T_{eff} derived for the primary component is by 300 K lower (see Table 2). The authors did not find evidence of the presence of a third body in the system, as supposed by Radhakrishnan et al. (1984) or Ribas et al. (2002).

We have chosen R CMa as our test star because of its luminosity ratio, $\frac{F_{\text{star}2}}{F_{\text{star}1}} \simeq 0.04$ in the visible, and because we can compare the results of our method with those obtained by Lehmann et al. (2018). The latter authors used high-resolution spectra of R CMa obtained with the HERMES spectrograph (Raskin et al. 2011). The spectra were reduced using the standard HERMES pipeline and, subsequently, normalized to the local continuum. Then the Fourier transformation-based KOREL program (Hadrava 1995, 2006) was used to disentangle the observed composite spectra. In fact, from a time series of spectra, the program delivers the decomposed spectra of the components, normalized to the common continuum of both stars, together with the optimum orbital elements, assuming pure Keplerian orbits. The spectra

of the components, resulting from observations in all out-of-eclipse phases, were renormalized to the individual continua with the help of the wavelength-dependent continuum flux ratio which was derived from spectrum analysis.

In our analysis we used the same HERMES normalized spectra used by Lehmann et al. (2018) and we applied our method to each j possible pair of $F_1(\lambda)$ and $F_2(\lambda, \phi)$ spectra. Thus, after every ERLICA run, i.e for each j pair of spectra, we checked the detection significance of the derived components, S_1^j and S_2^j . Then we properly averaged them to build $\langle S_1 \rangle$ and $\langle S_2 \rangle$, i.e., our final estimates of $F_{\text{star}1}$ and $F_{\text{star}2}$, respectively. In making the average of the second component estimates we used the $RV_{\text{star}2, \text{star}1}$ from Lehmann et al. (2018) to put all the individual S_2^j in the reference frame where $RV_{\text{star}2} = 0$. The results are shown in Figure 7: in the top panel we plot $\langle S_1 \rangle$ compared with the synthetic spectrum of the primary star computed using its atmospheric parameters given in (Lehmann et al. 2018, Table 1), in the middle panel $\langle S_2 \rangle$ is compared with the corresponding synthetic spectrum, and in the bottom panel we show $\langle S_1 \rangle$ and $\langle S_2 \rangle$ ACFs. To evaluate the detection significance we show in the bottom panel also the ACF of the *false* $\langle S_2 \rangle$ we obtained by using k pairs built with two spectra both taken during the secondary eclipse. As can be seen the $\langle S_1 \rangle$ and $\langle S_2 \rangle$ are in very good agreement with the corresponding synthetic spectra and their detection significance is $D_1 \simeq 59$ and $D_2 = \simeq 54$, respectively.

A comparison of our results and those obtained by Lehmann et al. (2018) using KOREL is shown in Figure 8. As can be seen there is a very good agreement for the Primary spectrum (with an rms value of 0.01) and a satisfactory agreement for the Secondary spectrum (rms = 0.10). The obtained rms values are of the same order of those between the derived spectra and the corresponding synthetic ones. We recall that the validity of the synthetic spectra is limited by the physics included in the corresponding models and by the different program codes used to calculate them. Figure 8 demonstrates that our method provides estimates of the disentangled spectra as reliable as those obtainable by well proofed programs used in binary star analysis.

In conclusion, combining the results of our simulations (see Section 3) and those obtained in the case of R CMa, we can say that the validity of our method is assessed.

4.2. The Case of 51 Peg

As shown in Section 3.1.2, to reliably disentangle individual components of binary systems using our ICA-based method, it is mandatory to have at our disposal spectra with very high S/N. This is particularly demanding in the case of exoplanetary systems which are characterized by a very low flux ratio (of the order of 1×10^{-4} or less); simulations (see Section 3.1.3) show that, for a typical case, an S/N > 5000 is required. To reach such an S/N is probably outside the possibility of the current instrumentation and certainly not available in currently public available data.

A way to mitigate such limitations with the aim of also successfully applying our method to such demanding systems is to try to increase somehow the S/N. This can be achieved, for example, by:

1. using averages of multiple spectra instead of single ones for the $F_1(\lambda)$ and $F_2(\lambda)$ in Equation (14) with the

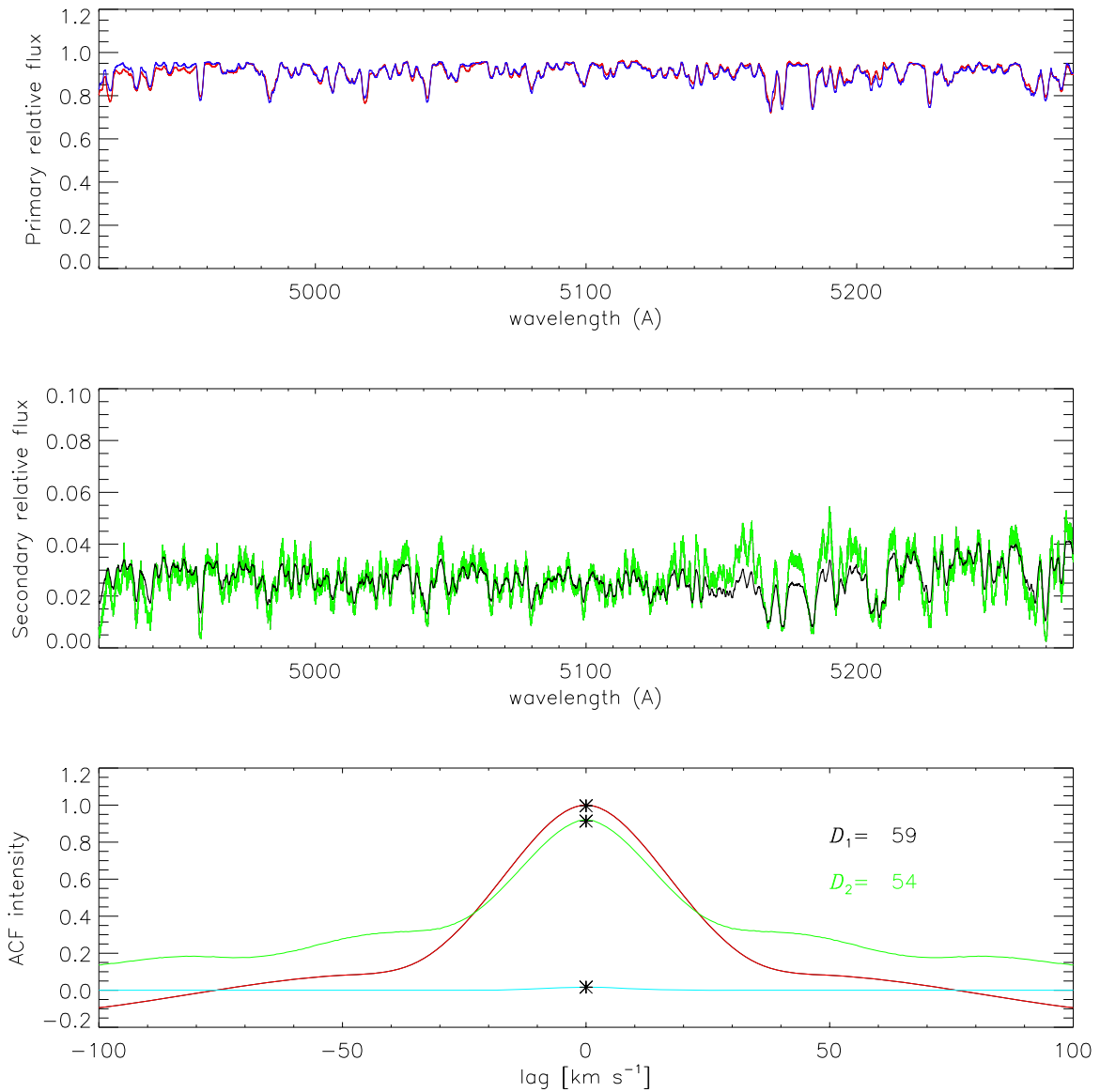


Figure 7. ICA results for the R CMa system: comparison between the extracted first component (red) and the synthetic spectrum of the primary star (blue)—upper panel; comparison between the extracted second component (green) and the synthetic spectrum of the secondary star (black)—middle panel; ACF profiles of averaged first (red) and second (green) components compared with the no-detection case (light blue)—lower panel.

constraint that they should be taken at exactly the same ϕ values;

2. using more than one pair of $F_1(\lambda)$ and $F_2(\lambda)$ and then averaging the retrieved components as done in Section 4.1.

Based on these considerations we decided to test our method on the real data of an exoplanetary system and in particular we decided to use 91 HARPS spectra of the system 51 Peg + 51 Peg b already used by Martins et al. (2015) and by Borra & Deschatelets (2018). The spectra were re-reduced by using HARPS DRS 3.4 and kindly made available to us by J.H.C. Martins. Martins et al. (2015), using the CCF method, and Borra & Deschatelets (2018), using the ACF method, detected from the analysis of these spectra the signal of 51 Peg b with a detection significance of $3.70 \sigma_{\text{noise}}$ and $5.52 \sigma_{\text{noise}}$, respectively.

We limited our analysis to the wavelength region $5400 \text{ \AA} < \lambda < 6800 \text{ \AA}$ where the spectra have $S/N > 200$. Unfortunately

this wavelength range is affected in several regions by the presence of telluric lines and removing them is not an easy task (see discussion in Smette et al. 2015). The method we applied is based on the fact that the HARPS spectra were obtained on different Julian days and, thus, they are affected by different heliocentric velocities. Therefore, after correcting all the spectra for the proper heliocentric velocity to put them in the wavelength laboratory rest frame, and after normalization, each spectrum shows the contamination of telluric lines at different wavelength positions (see upper plot in the upper panel of Figure 9). These wavelength positions can be easily identified by their anomalously large standard deviations with respect to the mean spectrum. Then, by sorting at each individual position the normalized flux of all the spectra, we separated the spectra which, in that specific point, have the higher signals from the others. The former are those less affected by telluric lines and their mean intensity value was used as an estimate of the telluric corrected flux value. Eventually, this value was adopted

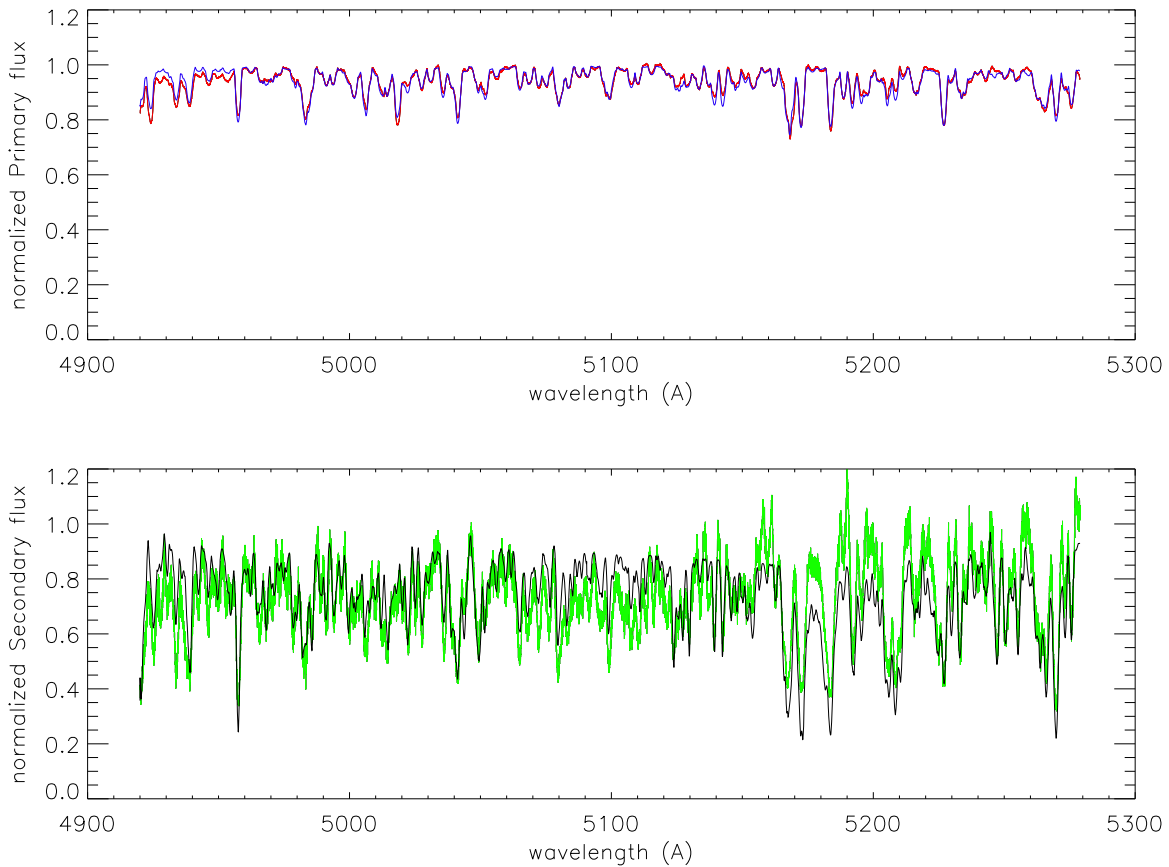


Figure 8. Comparison between the extracted spectrum of the Primary (top panel) and Secondary (bottom panel) of R CMa as obtained in this paper (red and green) and those obtained by Lehmann et al. (2018) (blue and black) using KOREL.

to substitute, at the corresponding wavelength point, the signal in the latter ones.

An example of the correction procedure in one of the regions affected by telluric lines is shown in Figure 9 where:

1. the upper panel shows three spectra and the differences from their mean before our telluric line correction;
2. the central panel shows the normalized sorted flux values at one of the λ in the region, $\lambda_0 = 6278.84 \text{ \AA}$. This plot is used to select the “uncontaminated” spectra (green dots) and to compute an estimate of the telluric corrected flux value at λ_0 (red line). The number of “uncontaminated” spectra, 12, is a good compromise obtained by visually inspecting several plots like that one shown;
3. the bottom panel shows the same three spectra of the left panel after the correction with, at the bottom, the new differences from their mean.

As can be seen the adopted method works quite well even if some residual contamination (of the order of a few percent in normalized fluxes) still remains in very critical regions (see lower plot in the bottom panel of Figure 9).

To perform our ERLICA analysis the 91 HARPS spectra were Doppler shifted for the RV_{star} values and divided into two groups:

1. Group 1: contains the 20 spectra that are near the inferior conjunction; they can be used, individually, as $F_1(\lambda)$ in Equation (14);
2. Group 2: contains the 71 spectra that are supposed to contain both F_{star} and F_{planet} since they have been

observed out of the inferior conjunction; they can be used as $F_2(\lambda)$ in Equation (14).

Now we are able to follow the steps outlined in Section 3.1. In particular:

- create the observed mixture X using for $F_1(\lambda)$ a spectrum pertaining to group 1 and for $F_2(\lambda)$ a spectrum of group 2 and apply ERLICA;
- fix signs and order of the extracted components S_{star} and S_{planet} to obtain estimates of F_{star} and F_{planet} ;
- compute the ACF of each component after re-sampling at steps of constant velocities;
- compute detection significance D_{star} and D_{planet} values.

With the aim of increasing the S/N we paired each of the 20 $F_1(\lambda)$ spectra individually with all the 71 spectra of group 2. Eventually we were able to apply ERLICA on $20 \times 71 = 1420$ mixtures X_j and for each j pair of $F_1(\lambda)$ and $F_2(\lambda)$ spectra, we obtained the S_{star}^j and S_{planet}^j estimates of F_{star} and F_{planet} . Moreover, to compute D_{star} and D_{planet} we applied ERLICA on the 190 k pairs built using as $F_2(\lambda)$ a spectrum of group 1 in order to check our F_{planet} estimate. In fact, in these cases we should not detect any signature from the planet and the analysis of the k obtained second ICA components can give estimates of possible “fake/spurious” S_{planet} introduced by ERLICA.

4.2.1. Results

Figure 10 shows the average ACFs of the S_{star}^j , S_{planet}^j , and “fake” S_{planet}^k . As can be seen the mean ACF of S_{star}^j shows that

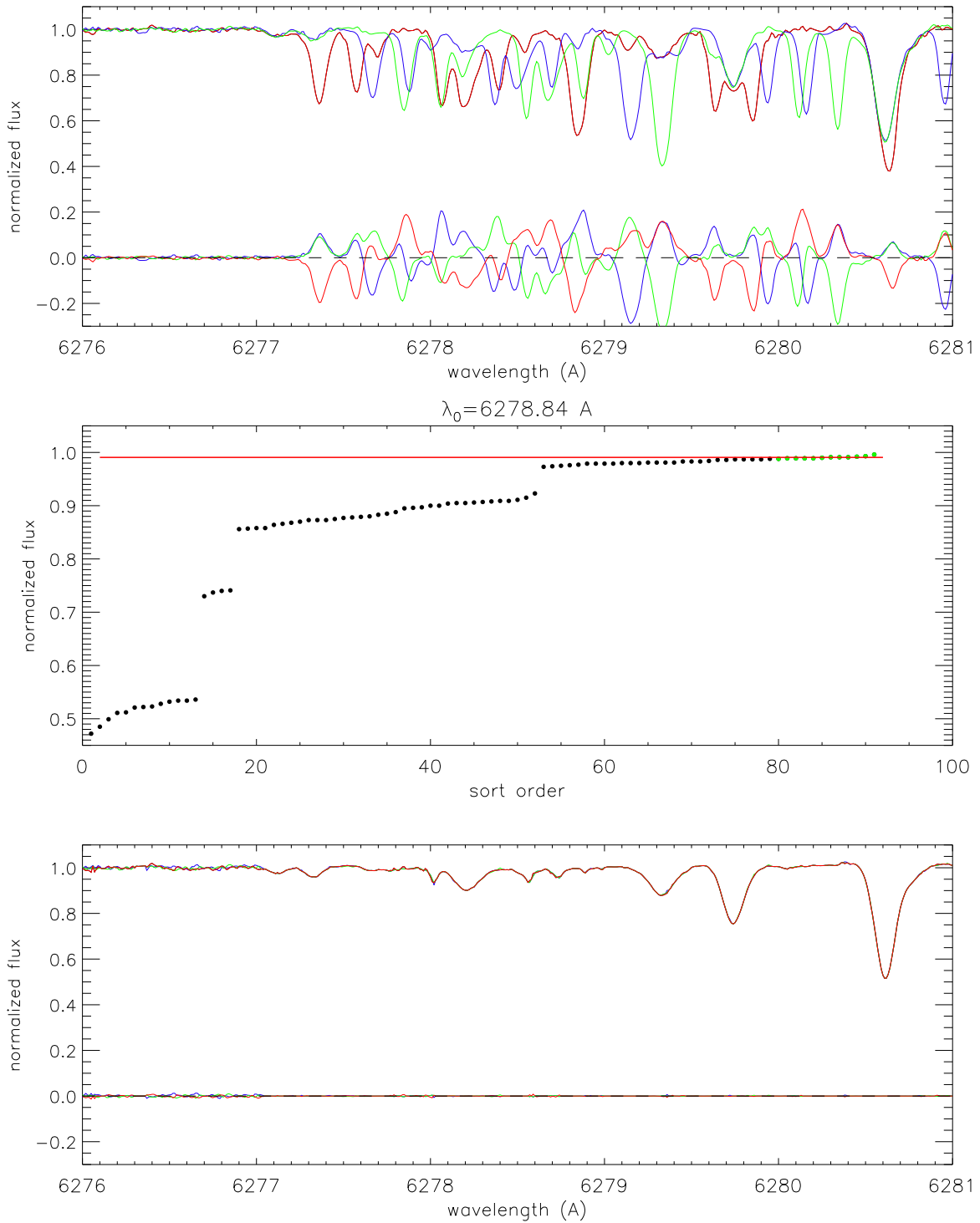


Figure 9. An example of the adopted telluric line correction: three spectra of 51 Peg obtained at different heliocentric velocities (red, blue and green) and the differences from their mean, before (upper panel) and after removing the telluric lines (bottom panel); the central panel shows the plot of the sorted fluxes used to select “uncontaminated” spectra (green points) and the estimated uncontaminated flux value (red line). See text for details.

our procedure derives a well defined S_{star} component which provides a very accurate estimate of F_{star} . The identification of S_{star} with F_{star} only is confirmed by the absence of any planetary signal if we apply to the S_{star}^j ACFs the same analysis used by Borra & Deschatelets (2018) to detect the signal from 51Peg b (see their Figure 7)

As far as the average ACF of the S_{planet}^j is concerned the computation of its detection significance, as described in Section 3.1.1 requires removal of the central peak. Actually

both the ACFs of the S_{planet}^j and of the “fake” S_{planet}^k show central peaks which extend from -2 to $+2$ km s^{-1} suggesting the presence of some correlated noise. Thus we removed this velocity interval before computing the gaussian fits shown by the blue and yellow lines in Figure 10. The obtained $D_{\text{planet}} = 2.3$ value is below our adopted detection threshold ($D = 3$) and this result is qualitatively in agreement with those obtained from our simulation (see Figure 3). In fact, even if we assume that our $F_1(\lambda)$, $F_2(\lambda)$ pairs are uncorrelated (which is

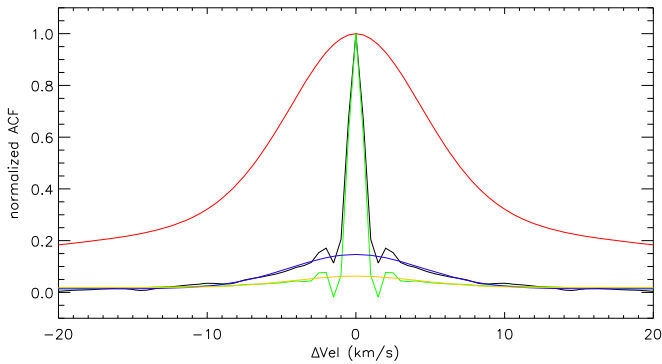


Figure 10. ACF profiles of average first (red) and second (black) components compared with the ACF of the “fake” second component (green). The blue and yellow lines are the fit of the black and green ACFs after removing the central points (see text).

quite unlikely) the S/N of our spectra, ~ 200 , should be multiplied by the square root of the number of pairs, $\sqrt{1420}$, leading to a value of S/N ~ 7500 which is slightly above the S/N limit from Figure 3. Thus, taking into account the not complete independence of our $F_1(\lambda)$, $F_2(\lambda)$ pairs and the different values of the S/N of the individual HARPS spectra, we can conclude that a low detection significance was expected. Furthermore the spectra coverage of the planetary orbit is neither complete nor homogeneous making the used HARPS data not an optimal set for our method (in particular we have very few spectra taken close to the superior conjunction or at phases near the maxima of $\text{abs}(\text{RV}_{\text{planet,star}})$). In any case, it is worthwhile noting that if we had used an estimator of detection similar to those used in the CCF and ACF approaches (for example the ratio between the peak of the fitted ACF and the standard deviation of the ACF pixel intensity for $\text{abs}(\Delta \text{vel}) > 10 \text{ km s}^{-1}$) we would have obtained $D_{\text{noise}} = 14.3 \sigma_{\text{noise}}$, i.e., a value larger than those obtained by Martins et al. (2015) or by Borra & Deschatelets (2018).

Even if the detection significance, D_{planet} , of the second component is quite low we tried to derive its wavelength dependence in order to understand its nature, i.e., if it contains the F_{planet} signature or if it is mainly due to systematics. To do that the individual S_{planet}^j estimates were averaged after applying the proper Doppler shifts to put them in a reference system where $\text{RV}_{\text{planet}} = 0$.

Figure 11 illustrates the final results:

1. in the top panel we plot in green the average estimate of S_{star}^j , the synthetic spectrum of 51 Peg used in Section 3.1 in light blue, and, to show the regions affected by telluric line contamination we may have not corrected perfectly, a scaled ($2\times$) telluric spectrum computed with SKYCALC⁵ in red;
2. the bottom panel contains the average estimate of S_{planet}^j in black, the average estimate of S_{star}^j in green, and the SKYCALC spectrum in red. The black curve was smoothed by using a 200 points running average to reduce the noise and shows some relatively broad features.

Whether the average estimate of S_{planet}^j is the real reflected signal from 51 Peg b is however questionable. In an attempt to answer to this question we compare in Figure 12 the average estimates of S_{planet}^j (black) with the “fake” S_{planet}^k (yellow),

derived from spectra in the inferior conjunction where the reflected F_{planet} signature cannot be present. Due to the centering and whitening of the input data and of the ambiguities intrinsic in ICA described in Section 2.3 we did not try to recover the absolute value of the black and yellow spectra and, therefore, both have zero mean value (in Figure 12 the spectra were vertically shifted to increase the readability).

As can be seen, there is a very low similarity between the star spectrum and the extracted and smoothed second component (see lower panel of Figure 11). In particular the strongest lines in the 51 Peg spectrum, i.e., the Na D doublet and H α are not present in the black curves of Figure 12. This is in contradiction with the expected results (see Figure 5) where the reflected signal should consist of the stellar spectrum modulated by the planetary albedo. On the other hand, the presence of more evident features and the corresponding larger standard deviations of the black curves with respect to the yellow ones in Figure 12 seems to suggest that we indeed detect some signal from 51 Peg b. If this is true a possible explanation for the absence of the stellar lines in our average second component could be the presence of clouds in the atmosphere of 51 Peg b which may smooth and flatten the planet reflected spectrum (see discussion, for example in Gao et al. 2017). Another possibility is that the “detected” features are the remnant of not completely removed telluric lines since the strongest of them fall in the critical regions where the SKYCALC spectrum shows most of the telluric lines (see Figure 12).

In conclusion, we do not have a sound final answer about the nature of the features in the average extracted second component. The possible detection of the reflected spectrum of 51 Peg b to be confirmed would require us to repeat our analysis using new “*ad hoc*” obtained input data, i.e., at higher S/N, covering the whole range of orbital phases, in particular both conjunctions, with more than one spectrum at each phase, and with auxiliary spectra to be used for accurately removing the telluric contamination.

5. Conclusions

In this paper we presented a new method based on applying the ICA technique for extracting the reflected planetary spectral signature from a series of composite spectra of a binary exoplanetary system. The main advantages, compared to the commonly adopted techniques like CCF and ACF, are that the extraction is “blind” i.e., it does not require any *a priori* knowledge of the underlying signals and that the method allows us not only to detect the presence of a planet contribution, but also to estimate its wavelength dependence.

To show and quantify the validity and effectiveness of the proposed approach, ERLICA, we applied it first to simulated data of an exoplanetary system with physical characteristics similar to 51 Peg + 51 Peg b. In Section 3.1.1 we introduced a quantitative estimator D of the detection significance to assess quantitatively the ERLICA disentangling capability. The results of the simulation showed that our method provides, in any case, an accurate estimate of the stellar spectrum and, when the noise in the input spectra is on the order or smaller than the planet signal, also the planetary albedo wavelength dependence.

Then we analyzed successfully the real case of an eclipsing binary star, the R CMa system, taking advantage of the fact that a binary star system could be considered physically similar to an exoplanetary system, but with a much higher flux ratio of the two components. The results for the spectra of the primary and secondary star showed that our method can be considered

⁵ <https://www.eso.org/observing/etc/bin/gen/form?INS.MODE=swspectr+INS.NAME=SKYCALC>

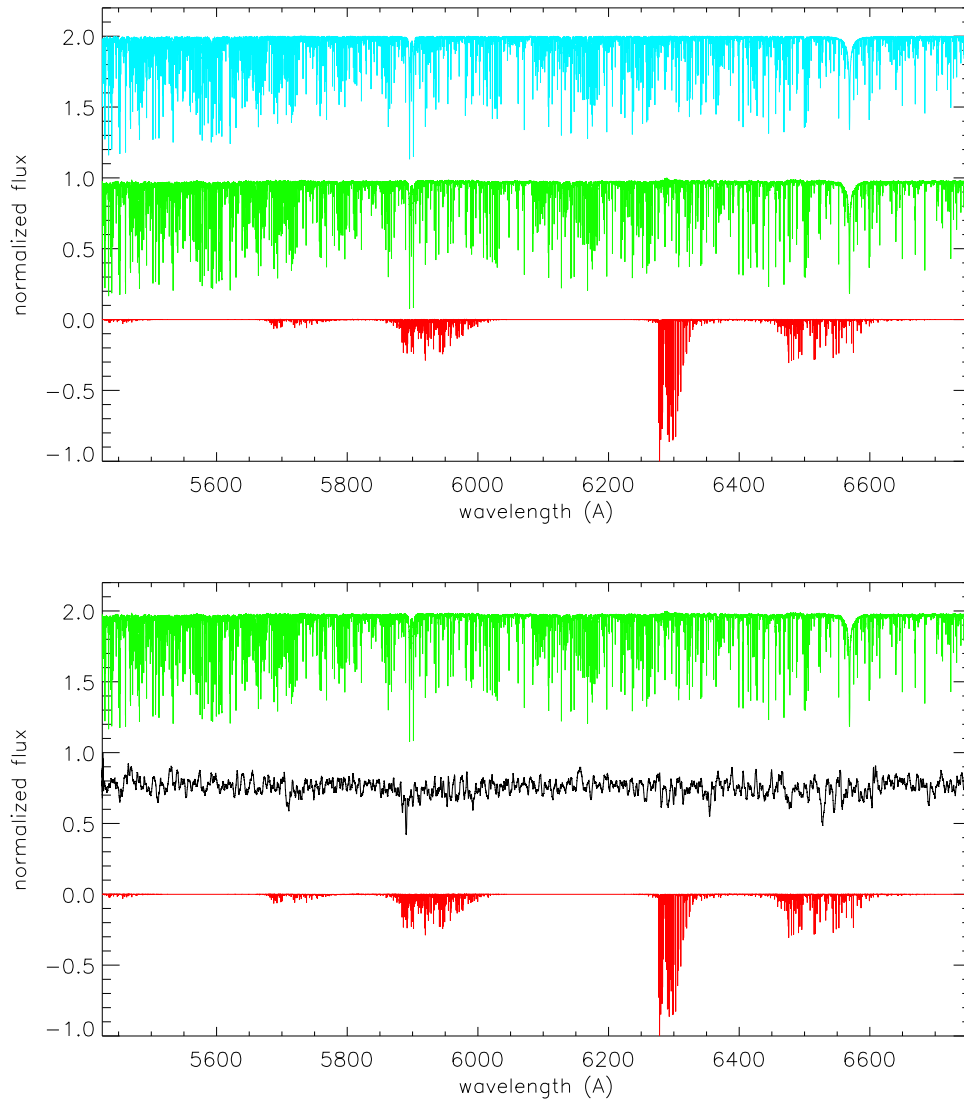


Figure 11. ICA results for the 51 Peg system in the range $5400 \text{ \AA} < \lambda < 6800 \text{ \AA}$. Upper panel: comparison among the extracted first component (green), the synthetic spectrum of the star (light blue), and a scaled ($2\times$) SKYCALC spectrum (red); lower panel: extracted and smoothed second component (black), extracted first component (green), and SKYCALC spectrum (red). The spectra are vertically shifted to increase the readability.

as a valid, and somewhat easier, alternative to well established codes for analyzing binary stars like e.g., KOREL, FDbinary (Ilijic et al. 2004) or Spectangular (Sablowski & Weber 2017).

Eventually we applied the method to real 51 Peg + 51 Peg b data. Also in this case we showed that our method is capable of extracting the stellar spectrum very effectively. As far as the detection of the planetary signal is concerned we obtained a quite low detection significance, $D_{\text{planet}} = 2.3$, although it is worthwhile pointing out that if we had used an estimator similar to those used by Borra & Deschatelets (2018) and Martins et al. (2015) we would have obtained a value which is larger than those obtained with the CCF or ACF methods.

Unfortunately, our attempts to analyze the wavelength dependence of the “possible” reflected spectrum of 51 Peg b to confirm its nature gave inconclusive results due to insufficient S/N and the absence of auxiliary data needed to accurately remove the telluric contamination. Therefore we could not definitively prove that we were able to derive the reflected spectrum of 51 Peg b.

In conclusion we can say that the proposed ERLICA approach could be considered, at least in perspective, a

powerful tool for studying and characterizing exoplanetary systems. In fact, we want to point out that this method will benefit significantly from the availability, in the near future, of new “*ad hoc*” scheduled observations obtained with the just coming into operation state-of-the-art instrumentation for exoplanetary research like ESO/VLT ESPRESSO (Mégévand et al. 2014), as well as with the foreseen instrumentation for the forthcoming 30 m class telescopes (like the High Resolution Spectrograph, HIRES, for the ESO ELT (Marconi et al. 2018)). In fact, these new instruments, due to their higher efficiency and telescope larger effective area, would allow us to obtain spectra with much higher S/N with the same exposure time than those used in this paper ($S/N_{\text{HARPS}} \simeq 200$, $S/N_{\text{ESPRESSO}} \simeq 500$, $S/N_{\text{HIRES}} > 9000$) as derived from the corresponding Exposure Time Calculators^{6,7} thus allowing us to fully exploit the ERLICA capabilities.

⁶ <https://www.eso.org/observing/etc/>

⁷ <https://www.arcetri.astro.it/~hires/etc.html>

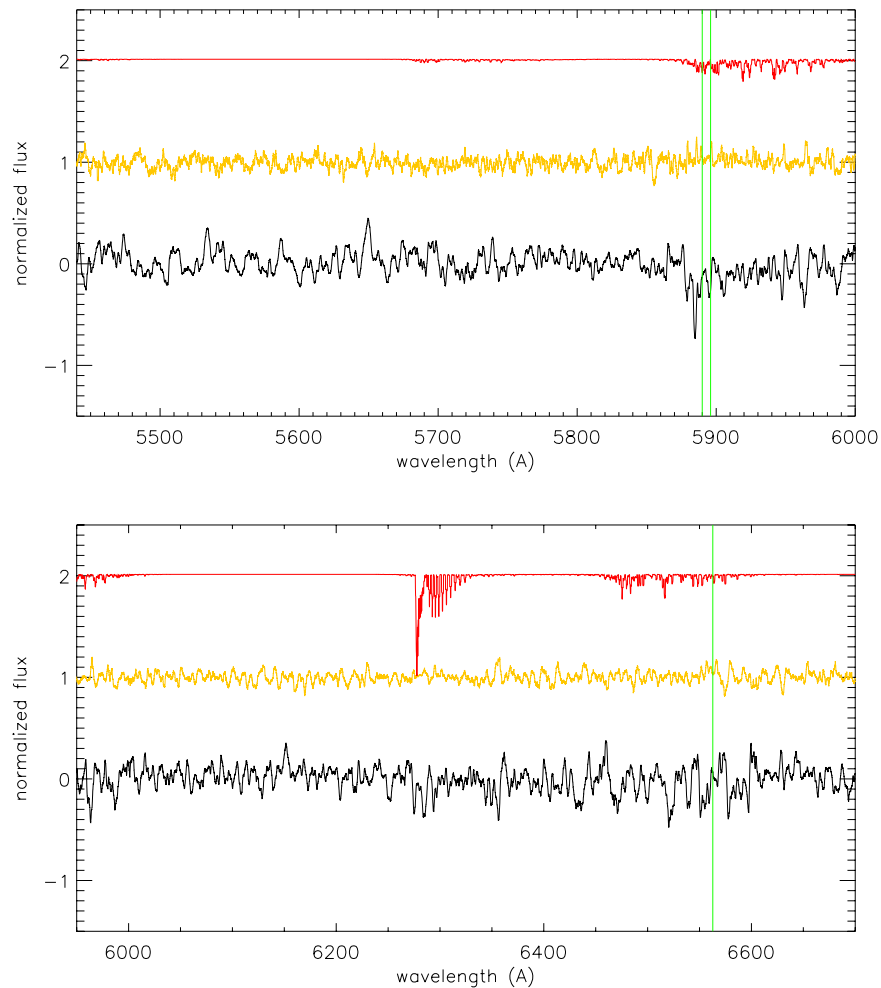


Figure 12. Average estimates of S_{planet}^j (black, possible F_{planet}) and S_{planet}^k (yellow, inferior conjunction, where the reflected F_{planet} signal cannot be present), and the SKYCALC telluric spectrum (red). The whole wavelength range was divided into two parts (upper and lower panels) and the spectra are vertically shifted to increase the readability. The three vertical lines show the laboratory positions of the Na D doublet lines and of $H\alpha$.

HL acknowledges support by the DFG grant LE1102/3-1. We want to thank J.H.C. Martins for providing us with the updated reduced data of 51 Peg. P.D.M. thanks the ESPRESSO Science Working Group 2 team and in particular M. R. Zapatero Osorio, N. C. Santos, F. Pepe, C. Lovis and D. Ehrenreich, for hints and fruitful discussions. We also thank several graduate students, in particular R. Bevilacqua and P. Menia, of the Università degli Studi di Trieste (Italy) who helped us, in the framework of their curricular internships, in setting the simulation used in this paper and in the analysis of R CMA.

Facility: ESO:HARPS.

Software: FastICA (v2.5; Hyvarinen 1999), ICASSO (v1.21; Himberg et al. 2004).

ORCID iDs

Paolo Di Marcantonio <https://orcid.org/0000-0003-3168-2289>

Carlo Morossi <https://orcid.org/0000-0002-3319-6375>

Mariagrazia Franchini <https://orcid.org/0000-0001-5611-2333>

Holger Lehmann <https://orcid.org/0000-0003-3449-4355>

References

- Belouchrani, A., Abed-Meraim, K., Cardoso, J., & Moulines, E. 1997, *ITSP*, **45**, 434
- Borra, E. F., & Deschatelets, D. 2018, *MNRAS*, **481**, 4841
- Budding, E., & Butland, R. 2011, *MNRAS*, **418**, 1764
- Cardoso, J. F., & Souloumiac, A. 1993, in *IEEE Signal Processing Workshop on Higher-Order Statistics* (Piscataway, NJ: IEEE), 275, <http://ieeexplore.ieee.org/stamp/stamp.jsp?tp=&arnumber=264552&isnumber=6642>
- Charbonneau, D., Noyes, R. W., Korzennik, S. G., et al. 1999, *ApJL*, **522**, L145
- Collier Cameron, A., Horne, K., Penny, A., & James, D. 1999, *Natur*, **402**, 751
- Donati, J.-F., Semel, M., Carter, B. D., Rees, D. E., & Collier Cameron, A. 1997, *MNRAS*, **291**, 658
- Fuhrmann, K., Pfeiffer, M. J., & Bernkopf, J. 1997, *A&A*, **326**, 1081
- Gao, P., Marley, M. S., Zahnle, K., Robinson, T. D., & Lewis, N. K. 2017, *AJ*, **153**, 139
- Gray, R. O., & Corbally, C. J. 1994, *AJ*, **107**, 742
- Hadrava, P. 1995, *A&AS*, **114**, 393
- Hadrava, P. 2006, *Ap&SS*, **304**, 337
- Hadrava, P. 2016, in *Astronomy at High Angular Resolution*, ed. H. M. J. Boffin et al. (Cham: Springer), 113
- Himberg, J., Hyvärinen, A., & Esposito, F. 2004, *NeuroImage*, **22**, 1214
- Hyvarinen, A. 1999, *ITNN*, **10**, 626
- Hyvärinen, A., Karhunen, J., & Oja, E. 2001, *Independent Component Analysis* (New York: Wiley)
- Ilijic, S., Hensberge, H., Pavlovski, K., & Freyhammer, L. M. 2004, in *ASP Conf. Ser. 318, Spectroscopically and Spatially Resolving the Components*

- of the Close Binary Stars, ed. R. W. Hilditch, H. Hensberge, & K. Pavlovski (San Francisco, CA: ASP), 111
- Karkoschka, E. 1998, *Icar*, 133, 134
- Kopal, Z. 1956, *AnAp*, 19, 298
- Kurucz, R. L. 2005, *MSAIS*, 8, 14
- Langford, S. V., Wyithe, J. S. B., Turner, E. L., et al. 2011, *MNRAS*, 415, 673
- Lehmann, H., Tsybal, V., Pertermann, F., et al. 2018, *A&A*, 615, A131
- Lindgren, L., & Dravins, D. 2003, *A&A*, 401, 1185
- Madden, J. H., & Kaltenecker, L. 2018, *AsBio*, 18, 1559
- Marconi, A., Allende Prieto, C., Amado, P. J., et al. 2018, *Proc. SPIE*, 10702, 107021Y
- Marley, M. S., Ackerman, A. S., Cuzzi, J. N., & Kitzmann, D. 2013, in *Comparative Climatology of Terrestrial Planets*, ed. S. J. Mackwell et al. (Tucson, AZ: Univ. Arizona Press), 367
- Marley, M. S., & Robinson, T. D. 2015, *ARA&A*, 53, 279
- Martins, J. H. C., Figueira, P., Santos, N. C., et al. 2018, *MNRAS*, 478, 5240
- Martins, J. H. C., Figueira, P., Santos, N. C., & Lovis, C. 2013, *MNRAS*, 436, 1215
- Martins, J. H. C., Santos, N. C., Figueira, P., et al. 2015, *A&A*, 576, A134
- McLaughlin, D. B. 1924, *ApJ*, 60, 22
- Mégevand, D., Zerbi, F. M., Di Marcantonio, P., et al. 2014, *Proc. SPIE*, 9147, 91471H
- Mortier, A., Faria, J. P., Santos, N. C., et al. 2016, *A&A*, 585, A135
- Radhakrishnan, K. R., Abhyankar, K. D., & Sarma, M. B. K. 1984, *BASI*, 12, 182
- Raskin, G., van Winckel, H., Hensberge, H., et al. 2011, *A&A*, 526, A69
- Ribas, I., Arenou, F., & Guinan, E. F. 2002, *AJ*, 123, 2033
- Rodler, F., Kürster, M., & Henning, T. 2010, *A&A*, 514, A23
- Rossiter, R. A. 1924, *ApJ*, 60, 15
- Sablowski, D. P., & Weber, M. 2017, *A&A*, 597, A125
- Smette, A., Sana, H., Noll, S., et al. 2015, *A&A*, 576, A77
- Valenti, J. A., & Fischer, D. A. 2005, *ApJS*, 159, 141
- Waldmann, I. P. 2012, *ApJ*, 747, 12
- Waldmann, I. P., Tinetti, G., Deroo, P., et al. 2013, *ApJ*, 766, 7
- Winn, J. N. 2010, in *Exoplanets*, ed. S. Seager (Tucson, AZ: Univ. Arizona Press), 55